

## A 32-channel time-resolved instrument for medical optical tomography

Florian E. W. Schmidt,<sup>a)</sup> Martin E. Fry, Elizabeth M. C. Hillman, Jeremy C. Hebden, and David T. Delpy

*Department of Medical Physics and Bioengineering, University College London, London WC1E 6JA, United Kingdom*

(Received 8 July 1999; accepted for publication 15 September 1999)

A prototype multichannel time-resolved medical optical tomography system is presented, and various instrumental aspects and performance issues are discussed. The instrument has been designed primarily as a continuous bedside monitor for obtaining functional images of premature infants' brains that are at an increased risk of injury due to dysfunction in cerebral oxygenation or hemodynamics. Separate maps of the internal absorption and scattering properties can be reconstructed from purely temporal measurements of photons transmitted diffusely through the tissue, and without recourse to reference or baseline measurements. The instrument employs 32 source fibers that sequentially deliver near-infrared pulsed laser radiation of picosecond duration. Transit time measurements of very high temporal resolution and stability are made between these sources and 32 detector optodes that are located on the surface. The effectiveness of this instrument is demonstrated by successfully imaging a tissue-equivalent phantom. © 2000 American Institute of Physics. [S0034-6748(00)02001-3]

### I. INTRODUCTION

In 1831, following an examination of a patient suffering from hydrocephalus, Richard Bright, a London physician, observed, "If a candle was held behind his head, or the sun happened to be behind it, the cranium appeared semi-transparent...".<sup>1</sup> Medical optical imaging technology has evolved considerably since those early days, and biomedical optics is now a fast growing field of research, both in academia as well as in industrial R&D laboratories. A prototype multichannel time-resolved optical tomographic imaging system has been developed at University College London (UCL) and it is introduced in this article in conjunction with initial images obtained from a tissue equivalent phantom.

Premature babies have an increased risk of cerebral hemorrhage, and both they and full term infants can suffer from blood flow or oxygen deficiencies (hypoxic ischemia) leading to severe neurodevelopmental disorders. There is currently no device capable of *continuously* imaging cerebral blood volume and oxygenation at the bedside. Hence research at UCL has focused on the development of an instrument which employs near-infrared (NIR) laser light for imaging the neonatal brain, and that is capable of detecting and studying the consequences of brain pathologies as well as monitoring response to treatment. Optical tomography may prove a useful tool to complement existing medical imaging modalities since it employs harmless, nonionizing radiation so that patients can be examined repeatedly, or even continuously. It provides a means to image and quantify functional changes in cerebral blood volume or oxygenation, thereby revealing important physiological information *before* irreversible structural damage occurs.

NIR tomographic imaging is in many ways an extension of near-infrared spectroscopy,<sup>2-4</sup> which is an established technique that primarily aims to measure global changes in tissue oxygenation and blood volume. While scattering is the dominant interaction mechanism of NIR light with tissue, the important physiological information is derived largely from the level of absorption. Human tissue is nearly transparent to NIR light, and the most significant absorbers are water (which represents a constant background) and hemoglobin, the oxygen carrier in the red blood cells. Hemoglobin is a natural contrast agent that allows estimates of tissue oxygenation to be made by measuring the absorption at two wavelengths, ideally at either side of 800 nm where the absorption spectra of oxygenated and deoxygenated hemoglobin intersect. Variation in myelination may also be evident as differences in scatter.

There are various approaches to optical imaging through tissue which have been reviewed by Hebden *et al.*<sup>5</sup> and by Arridge and Hebden.<sup>6</sup> The types of instruments can be broadly divided into the following three groups.

*Continuous intensity instruments*, which measure changes in transmitted intensity due to variation in attenuation between the detector and source. Examples include a system described by Maki *et al.*<sup>7</sup> that performs *topographic* mapping (as opposed to tomographic transillumination imaging) of the cortex in response to various stimuli, and the continuous intensity light imager developed by Chance *et al.*<sup>8</sup> Colak *et al.*<sup>9</sup> have also reported a tomographic mammography system.

In *intensity-modulated instruments* a source of light (typically a current modulated diode laser) is modulated at radio frequencies, and the detected intensity ( $I$ ), phase shift ( $\Phi$ ), and modulation depth ( $M$ ) relative to the input signal are measured. Jiang *et al.*<sup>10</sup> reported reconstructions of phantom images from such frequency-domain measurements, and

<sup>a)</sup>Electronic mail: florian@medphys.ucl.ac.uk

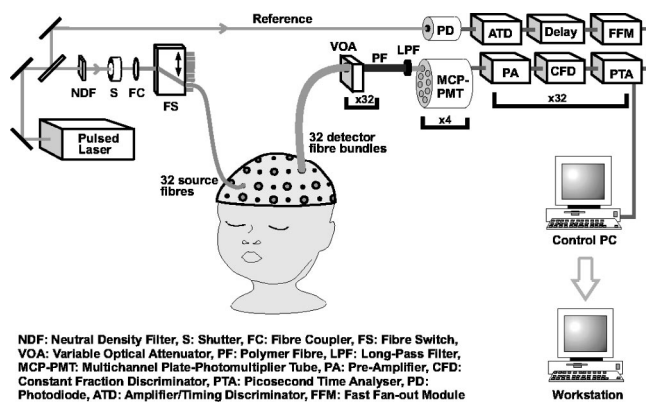


FIG. 1. Schematic diagram of the imaging system. Note that only one source fiber and one detector fiber bundle are shown for clarity.

Kaschke *et al.*<sup>11</sup> have built a frequency domain mammography system.

For *time-resolved instruments* the temporal response to an ultrashort (typically a few ps) input laser pulse is measured. The temporal distribution of light emerging from the tissue surface, conventionally referred to as a temporal point spread function (TPSF), is usually detected with either a synchroscan streak camera, or a time-correlated single photon counting (TCSPC) system. In the latter case a photon counting detector measures the flight times of individual photons relative to a reference pulse. The advantages of TCSPC versus streak camera systems include a larger detector area and a significantly better temporal linearity and dynamic range. Various time-resolved systems have been proposed and evaluated. These include a system based on an optical time domain reflectometer (OTDR) developed by Benaron's group,<sup>12</sup> a streak camera system,<sup>13</sup> and 64-channel,<sup>14</sup> 8-channel,<sup>15</sup> and single channel scanning<sup>16</sup> TCSPC instruments.

Past attempts to image through human tissue with light have only had limited success because of the highly diffuse propagation of optical radiation through thick sections of tissue (see, for example, Müller *et al.*<sup>17</sup>). Extracting information encoded in a set of TPSFs recorded with a time-resolved instrument represents one possible approach to overcoming these limitations, and a system designed for this purpose is described here. Furthermore, since our previous experience indicates that measurements of the absolute transmitted intensity are very difficult in a nonlaboratory (i.e., clinical) environment, we restrict ourselves to purely time-resolved measurements. Accurately recording intensity is difficult because of the very strong sensitivity of the detected intensity to photon interactions at the surface, for instance, due to a hair trapped between skin and optode. In contrast, temporal (or frequency-domain) data are more sensitive to regions deep inside the tissue and are therefore inherently more robust.<sup>4</sup>

## II. SYSTEM DESCRIPTION

Preliminary descriptions of the 32-channel UCL system during its development have been provided by Wells *et al.*<sup>18</sup> and by Schmidt *et al.*<sup>19</sup> Figure 1 shows a schematic diagram

of the final instrument's principal optical and electronic components. The laser source produces high energy picosecond pulses at adjustable wavelengths. A neutral density filter is used to attenuate the light to the desired level. The laser beam then passes through an electronically controlled shutter and a beam splitter, and is coupled into a  $1 \times 32$  fiber switch. The 32 output source fibers are held in contact with the surface of the object (e.g., the head of a neonate) and illuminated *sequentially*. As the photons pass through the tissue they undergo multiple scattering and are dispersed in time. Photons exiting the surface are *simultaneously* collected by 32 large diameter detector fiber bundles arranged over the surface of the head. Thus the source is effectively moved over the head in discrete steps by coupling light sequentially into one of the 32 source fibers, while 32 detector fiber bundles simultaneously collect light exiting the tissue and relay it to 32 fully simplex ultrafast TCSPC detectors. Since there is a large variation in source-detector fiber separation there is a correspondingly very large dynamic range of intensities of light emerging from the tissue surface. A set of 32 computer controlled variable optical attenuators (VOAs) ensures that the intensity of detected light does not saturate or damage the detectors, and the flux of photons is sufficiently small to prevent detection of multiple photons during each cycle (single photon counting limit). Attenuators are left fully open for detector fiber bundles that are sufficiently distant from the source.

Light passing through each VOA is collected by a short single polymer fiber and relayed to the photocathode of one of four 8-anode multichannel plate-photomultiplier tube (MCP-PMT) detectors via a visible light blocking long pass filter. The resulting analog electronic pulses are then preamplified and converted into fast nuclear instrument module (NIM) logic pulses with high timing accuracy by the constant fraction discriminator (CFD). Meanwhile, reference pulses are split off the main laser beam with a beamsplitter and used to illuminate a fast photodiode. The resulting electronic pulses are preamplified and converted into fast NIM logic pulses by the combined amplifier/timing discriminator (ATD) unit. The delayed reference pulses and the signal pulses from the CFD are then used by the picosecond time analyzer (PTA) unit to measure the relative arrival times of individual photons. The PTA automatically builds up a histogram of photon flight times (a TPSF) which is read out by a control PC. These TPSFs can be interpreted as the impulse response of the tissue for a given source/detector combination. The full set of TPSFs for all source-detector combinations represents the raw image data, and is transferred to a fast UNIX workstation for the reconstruction of absorption and scattering maps (see Sec. V C).

The whole imaging system was designed to be rugged and portable to enable it to be placed at the bedside in a clinical environment. Figure 2 shows a photograph of the instrument, which has become commonly known as multi-channel opto-electronic near-infrared system for time-resolved image reconstruction (MONSTIR). The individual components are described in more detail below.

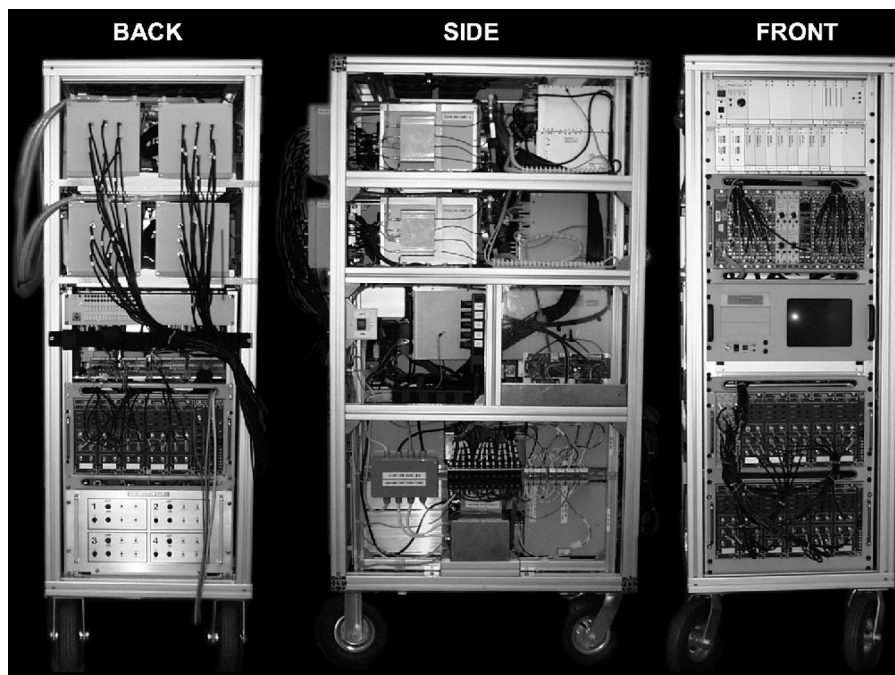


FIG. 2. Photograph of the instrument's portable main rack, which contains all components apart from the laser source and MCP-PMT cooler unit. Most of the electronics and the control PC are housed on the front of the 19 in. rack. The VOAs (four boxes containing eight units each) and the fiber switch are located at the back, while the MCP-PMT cooling houses can be seen in the top part of the side view.

### A. Optical components

The optical components of the system were designed for minimal dispersion (and hence maximal temporal resolution), optimum amount of light detected, as well as flexibility and ruggedness. Care was taken to ensure minimum stray light entry and reflections within the whole optical assembly.

The laser source used for laboratory studies is a Spectra-Physics (Mountain View, CA) Ti:sapphire Tsunami system pumped by a Millennia diode-pumped continuous intensity laser. It operates at approximately 80 MHz and produces NIR picosecond pulses with an average power of  $\sim 700$  mW at 800 nm. The reference signal is derived from a fast (rise time  $\sim 500$  ps) photodiode (S4752 PIN) supplied by Hamamatsu Photonics (Hamamatsu City, Japan). Important optical components and their technical specifications are illustrated in Fig. 3. Custom-built VOAs control the light level incident onto the detectors by selectively obscuring a varying fraction of the detector fiber bundle aperture. A range of holes of different diameters (0.2–3.5 mm), providing a range

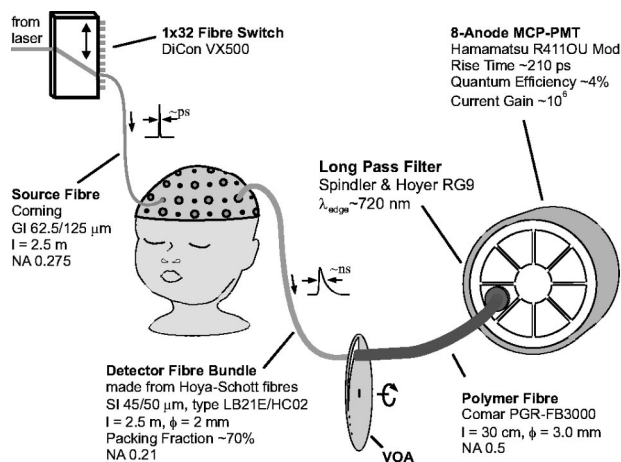


FIG. 3. Illustration of the main optical components.

of discrete attenuation values, and a slit of varying width, for continuous adjustment of the attenuation, are etched into a blackened  $100 \mu\text{m}$  stainless steel disk that is positioned by a computer controlled stepper motor. This low-cost, compact and rugged design provides wavelength-independent attenuations up to about 3 optical densities (ODs). The polymer fibers have a large diameter and numerical aperture (NA) in order to maximize collection of light passing through the VOAs. They have been chosen because of their mechanical flexibility, the lack of a packing fraction loss (as compared to a fiber bundle), and because they act as diffusers to ensure uniform illumination of the detector photocathodes. Being only about 30 cm in length the temporal dispersion they contribute ( $< 30$  ps) is acceptable. The detectors are customized ultrafast MCP-PMTs supplied by Hamamatsu Photonics. Apertures in front of the MCP-PMTs ensure that illumination of the photocathode is only about 5.5 mm in diameter and  $\geq 1.0$  mm from the individual anode boundaries. The detectors are cooled to approximately  $-25^\circ\text{C}$  by water-cooled Peltier elements in order to effectively eliminate dark counts. The operating voltage is typically  $-3.2$  kV.

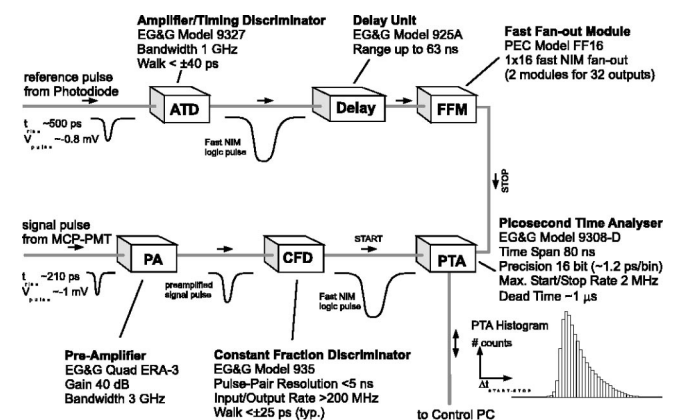


FIG. 4. Schematic of the pulse-processing electronics.

### B. Electronic components

Each photon detected by a MCP-PMT produces an electronic pulse whose arrival time is measured using pulse processing electronics (see Fig. 4) supplied by EG&G ORTEC (Oak Ridge, TN). The system is operated in reverse start-stop mode, such that the MCP-PMT pulse provides the start and the (delayed) repetitive laser reference pulse the stop signal. This is more efficient since for typical count rates of  $\sim 100\,000$  cps at a laser repetition rate of  $\sim 80$  MHz over 99% of laser pulses will not produce a corresponding count. Operating in reverse start-stop mode thus ensures that every start pulse receives a stop pulse. Hence photons that are detected, amplified and discriminated before reaching the PTA's start channel are timed precisely relative to a fixed event (the laser pulse).

The PTAs, which record the timing histograms from multiple start events, are high-resolution and wide dynamic range time-to-digital converters, whose technology is based on an electronic vernier scale arrangement.<sup>20</sup> It should be noted that in practice the maximum count rate of the system in its current configuration is limited to approximately 300 000 cps by the PTA's processing speed. This is well within the single photon counting requirements and sufficient given that the number of detectable photons transmitted through thick sections of tissue is generally less at safe laser exposure levels.

### C. Instrument control

A controlling PC (Pentium 90 processor, 64 Mb of memory) reads and processes the recorded TPSFs, and controls all other hardware in the system. The instrument control software, which was developed using Borland Delphi 3.0 and runs under Windows 95, enables the imaging system to be fully automated. Its functions include hardware control [PTAs, VOAs, fiber switch, MCP-PMT high voltage power supply unit (PSU), Peltier cooler PSU, laser shutter], as well as acquisition, processing and display of the measured data. The ambient, system and MCP-PMT temperatures, as well as the Peltier cooling circuit flow speed, are constantly monitored. Various electronic and software based safety mechanisms have been integrated in order to protect the patient and the MCP-PMT detectors. An electronic system integrity monitor, which incorporates a "watchdog" timer circuit, provides a computer-independent safety mechanism that is able to trigger an automatic system shutdown. In addition, a manual override switch allows the operator to instantly set the system into a safe state (close laser shutter, power down MCP-PMT PSUs, etc.).

### III. TEMPORAL CALIBRATION

Because, as explained earlier, absolute intensity is not considered a viable measurement for optical tomography, no attempt is made to calibrate for the variation in detection efficiency. However, accurate temporal calibration is essential in order to take into account the variation of the delay in the optical fibers, electronic cables, etc. In addition to calibrating temporal delays, the measurements described here also allow correction of the finite temporal response of the

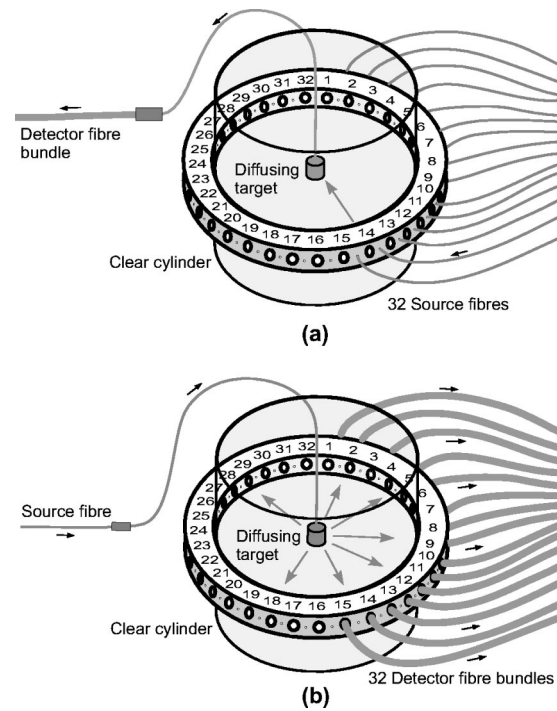


FIG. 5. Source calibration: (a) all 32 source fibers are arranged around the circumference of a clear cylinder and illuminated sequentially. Detector calibration: (b) all 32 detector fiber bundles are illuminated simultaneously by a source at the center. Note that for clarity not all fibers are shown.

system for all source-detector combinations. Three separate calibration measurements are performed (described in Secs. III A–C), and the resultant data are used to perform the relevant corrections outlined in Sec. V B. A dedicated reference channel for continuously monitoring delay variations throughout experiments is not required in this system.

#### A. Source calibration measurement

The source calibration accounts for the *relative* differences in the lengths of the source fibers. Figure 5(a) illustrates the tool used to perform this calibration. The 32 source fibers are arranged around the circumference of a clear cylindrical block made of epoxy resin. One source is illuminated at a time. A small diffuser at the center receives a fraction of the light injected into the cylinder, and some is transmitted into a collecting fiber. This collecting fiber is connected to a detector fiber bundle that allows a temporal profile to be recorded.

#### B. Detector calibration measurement

The same tool described above is used for performing an equivalent *relative* calibration of all the detector channels

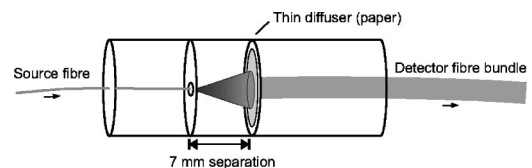


FIG. 6. Absolute calibration: a source fiber and detector fiber bundle are placed at a known separation from each other.

[see Fig. 5(b)]. In this case light is injected via a source fiber into the diffuser at the center of the clear cylinder. All 32 detector fiber bundles are arranged around the circumference of the cylinder so that the photon flight times from the center to the detector fiber bundles are equal. The bundles simultaneously collect light radiated from the center. As will be discussed in Sec. VB these measurements then allow calibration for the relative delay due to the detector fiber bundles, coaxial cables and electronic pulse-processing equipment.

### C. Absolute calibration measurement

An *absolute* calibration is performed to determine the absolute temporal delay for a particular source-detector pair. This single measurement, combined with the relative source and detector calibrations outlined above, permits the absolute temporal offsets for *all* source-detector combinations to be computed. The absolute calibration tool is illustrated in Fig. 6. A source fiber is positioned at a known separation (7 mm) from the detector fiber bundle, such that it illuminates its full aperture. The additional temporal delay due to this separation is included in the calibration process. A piece of paper is placed against the tip of the detector fiber bundle and illuminated by the beam emanating from the source fiber. The paper diffuses the light sufficiently to ensure uniform excitation of all modes in the fiber bundle, comparable to illumination with diffuse light exiting the tissue in an imaging experiment.

## IV. SYSTEM PERFORMANCE

There are a number of different technical aspects that need to be considered when evaluating and optimizing the performance of a time-resolved tomography system. These include the data acquisition efficiency, temporal accuracy and stability, as well as various systematic errors that may affect the quality of the measurements.

### A. Data acquisition efficiency

The time required to obtain sufficient signal depends on various factors including the thickness of the tissue to be imaged, the incident laser power and the photon detection efficiency of the instrument. Since the MCP-PMT detectors are cooled there are negligible dark counts (typically <10 cps). Therefore shot (Poisson) noise and stray room light entering the detector are the only sources of random noise in the measurement. All 32 detector channels are fully simplex so that only the sources need to be multiplexed. Hence the total data acquisition time of an imaging experiment equals the acquisition period per source position plus the time required to switch between source positions multiplied by the total number (32) of source positions. The system is fully computer controlled, and it currently takes about 3.5 s to switch between adjacent sources. The operations that are required during this period include (i) advancing the fiber switch, (ii) adjusting the VOAs in order to re-balance the detected intensities, (iii) reading the data (TPSFs) from the PTA units, as well as resetting them in preparation for the next acquisition, and (iv) some basic processing of the raw

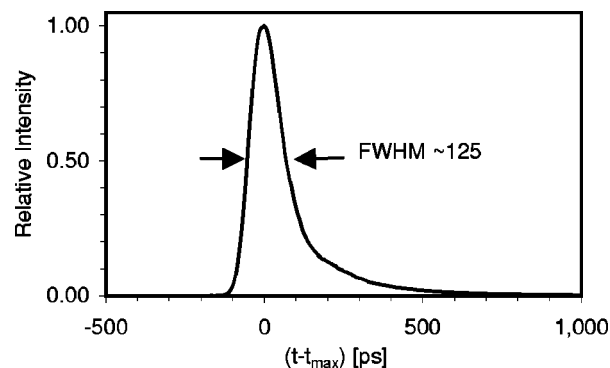


FIG. 7. A typical IRF recorded using the absolute calibration tool.

data. The data are saved to disk as binary files while the next acquisition is being performed. It is estimated that with further optimization of the software the switching time could be decreased to about 1 s.

The photon collection efficiency of the system is strongly influenced by many factors including the finite numerical aperture (0.21) of the detector fiber bundle, the quantum efficiency of the MCP-PMT detector ( $\sim 4\%$ ), as well as losses within the fibers (absorption, surface reflections, packing fraction, etc). Furthermore, efficiency is also limited by the photon counting electronics. The PTA, and to a lesser extent the MCP-PMT, saturates slightly at high count rates. For typical count rates of the order of 100 000 cps this corresponds to a loss of only a few percent, which may however require calibration when intensity measurements are performed.

Recent experiments with tissue-equivalent phantoms suggest that in order to obtain adequate photon statistics the acquisition time is typically 15–30 s per source for an incident laser power of the order of a few mW. Combined with a source switching speed of 3.5 s this corresponds to a total acquisition time for a complete scan of approximately 10–20 min with around  $10^5$ – $10^6$  photons per TPSF. However, the tolerance of the reconstruction algorithm to lower photon counts has yet to be established.

### B. Instrument response

The quality of the TPSFs, and hence that of the reconstructed image, depends to a large extent on the system's temporal response. The instrument response function (IRF) of the *overall* system is measured by directly connecting the source and detector fibers, and recording a histogram of photon flight times. Keeping the width of this distribution to a minimum is an important design consideration and it poses a major technological challenge. Components that mainly contribute to temporal broadening are the detector fiber bundle, polymer fiber, MCP-PMT detector and processing electronics, whereby optimal adjustment of the CFD walk and threshold settings was found to be critical. The picosecond laser source and the graded-index source fiber cause negligible broadening. Note that the contributions from the individual components of the system are convolved, so that the overall full width at half maximum (FWHM) can be estimated by adding these contributions in quadrature. A sample

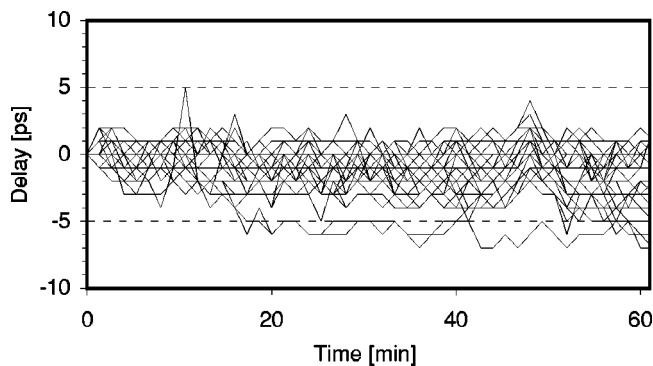


FIG. 8. Graph illustrating the temporal drift in 32 channels over a 1 h period.

IRF, recorded with the absolute calibration tool described in Sec. III C is shown in Fig. 7. Note the asymmetry of the curve, which is most likely due to intermodal dispersion in the optical fibers. The IRF FWHM of the 32 channels is typically in the range of 80–150 ps.

### C. Temporal stability

The timing accuracy and stability of the system are of fundamental importance when attempting to obtain high-quality data. This is because the initial temporal calibration of the system must be assumed to remain valid throughout the imaging experiment, which in the case of continuous clinical monitoring may be up to several hours. There are numerous causes of temporal drift and jitter, and various measures have been invoked to eliminate or reduce these to acceptable levels.

The method employed here to evaluate the temporal stability of the system is to repeatedly perform a detector calibration, outlined in Sec. III B, and plot the pulse arrival time (defined by the peak position derived from a polynomial fit to the recorded time curve) for each measurement and all channels as a function of time. Figure 8 shows such a plot, recorded over a 1 h period after allowing the instrument to stabilize. The delay has been arbitrarily set to 0 ps at time=0 min, and is recorded relative to this reference for each channel. Data points were recorded every 90 s, with each acquisition lasting 10 s. The system can be seen to be highly temporally stable in this experiment. Typically the drift (slow variation in delay) is approximately 5 ps/h, and the jitter (erratic point to point variation in delay) around the same magnitude.

Before the system had been optimized, we observed drift and jitter of up to hundreds of ps. Eliminating this problem was a major task, and it has been the focus of a considerable effort over the past 12 months. The measures taken to achieve the current level of stability included the following.

- (1) *System warmup.* A minimum warmup time of approximately 10 h is required. Ideally the system is left switched on permanently.
- (2) *Temperature fluctuations.* Fluctuations of a few degrees in the ambient temperature can cause measurable temporal drift or jitter that is believed to be primarily due to phase delays in the coaxial signal cables. Keeping tem-

perature fluctuations during the experiment to a minimum by ensuring a relatively stable system temperature and shielding or enclosing the cables and electronics in a stable unit help reduce drift and jitter. Furthermore, minimizing cable lengths reduces these effects, and it may also be advisable to choose cable types that have been designed to exhibit small phase delay variations with temperature.

- (3) *PSU stability and noise.* Power supply stability is important since supply voltage variations can affect the timing properties of the pulse-processing electronics. The system incorporates a combination of linear and switch-mode PSUs. Since switch-mode PSUs are inherently very noisy, their output cable lengths have been minimized. Screening is employed and ferrite filters are fitted throughout the system to reduce the radiation and pickup of high-frequency noise, which has been found to interfere with the pulse-processing equipment.
- (4) *Wiring and grounding.* The system has been rewired such that the mains/power cables are located on one side and the signal lines on the other side of the rack where possible. A rigorous grounding scheme for all components has been installed.
- (5) *Electronic connectors.* Significant jitter of several hundred ps can be caused by poor electronic connections between components resulting, for example, from loose fitting and dry joints. The system employs a combination of Lemo, BNC and SMA connectors. Cable flexure, especially when the cable is fitted with a poor connector, also has a measurable effect.
- (6) *Laser pulsing stability.* Laser pulsing instability (random variations of the laser pulse width from the normal  $\sim 1$  ps up to several hundred ps) causes significant jitter. Moreover, laser instability usually demands re-alignment of the laser optics, which in turn may necessitate re-calibration of the imaging system.
- (7) *Reference photodiode.* Optimum reference photodiode operating conditions (the supply voltage and illumination level) are important. It was found that a small drift in the incident laser power (a few %/h) can translate into a measurable temporal drift of the reference signal.

### D. Cross talk

Two distinct types of cross talk are relevant to the imaging system. The first is that originating within the 8-channel MCP-PMTs. The anodes of the MCP-PMT are arranged in eight segments as shown in Fig. 3, and cross talk is appreciable only for channels that are physically adjacent. This type of cross talk consists of electronic and optical components, the latter being minimized by careful positioning of the polymer fiber and the aperture in front of the photocathode, described in Sec. II A. It is typically less than 0.3% in terms of count rate and, at this stage, is not known to have a significant effect on the quality of the data. It should be noted that cross talk between detectors is another reason to employ the variable optical attenuators for balancing intensities between the different channels. If adjacent channels have very different count rates the effect of cross talk be-

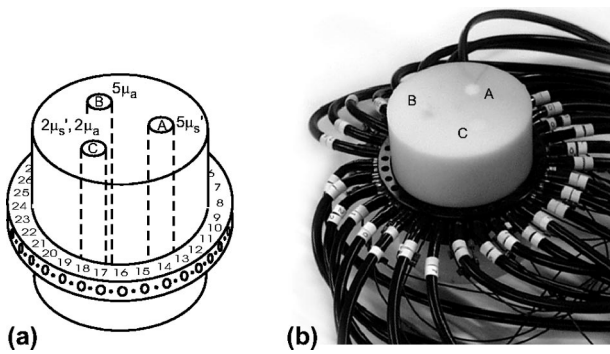


FIG. 9. Illustrative diagram (a) and photograph (b) of the solid tissue-equivalent phantom with the fiber holder ring. Note the small-diameter source fibers which are interspersed between the large-diameter detector fiber bundles (b).

comes significant in the channel with the lower count rate.

A second type of cross talk has been found to originate in the fiber switch, which connects the input fiber (from the laser) with any one of 32 source fibers that are attached to the tissue surface. Although the cross talk between channels in the switch is only  $< 10^{-8}$  (the manufacturer's specification), this fraction is comparable to the attenuation produced by several centimeters of tissue. Thus light entering the tissue from nonactivated sources very close to a given detector may provide a signal that is significant compared to that due to an activated source that is much further from the detector. The consequence is a narrow peak which precedes the arrival of the desired TPSF, because light leaking from an adjacent source travels a much shorter distance to the detector. However it can be removed through data processing by rejecting any signal prior to the main TPSF. Nonactivated sources that are not very close to the detector should not contribute an appreciable signal because the light has to travel through substantial thicknesses of tissue and is therefore sufficiently attenuated.

### E. Reflections

Optical reflections represent a potentially significant source of systematic error. Multiple stray reflections in the optical system can be avoided through effective shielding, but reflections occurring at interfaces within the optical fibers are more difficult to eliminate. For such a reflection to affect the measurement it must have a roundtrip time short enough ( $\leq 7$  ns) to overlap the TPSF to be measured. Hence fibers have been chosen to be sufficiently long, angle-polished and with coupling gel between interfaces where possible. However, the short ( $\sim 30$  cm or  $\sim 3$  ns roundtrip time) single polymer fiber between the VOA and the MCP-PMT produces an internal reflection of the order of 0.5%, which can affect the measurements. It must therefore be considered when the raw TPSF data are pre-processed for image reconstruction.

## V. IMAGING EXPERIMENT

An imaging experiment using a solid tissue-equivalent phantom was performed to evaluate the performance of the system. This phantom is made of epoxy resin with scattering

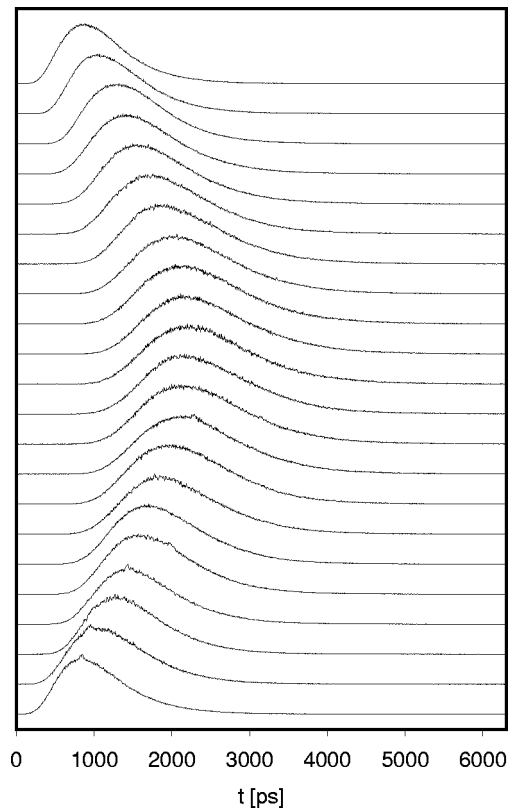


FIG. 10. TPSFs representing the image raw data for one source position. There are 22 measurements because 5 detector channels to either side of the source are blocked by the VOAs.

titanium dioxide particles with a near-infrared absorbing dye added to provide a transport scattering coefficient  $\mu'_s = 1.0 \pm 0.02 \text{ mm}^{-1}$  and an absorption coefficient  $\mu_a = 0.01 \pm 0.002 \text{ mm}^{-1}$ . The refractive index of the resin is  $n = 1.56 \pm 0.01$  at a wavelength of 800 nm. A recipe for making this type of phantom and establishing its optical parameters has been described by Firbank *et al.*<sup>21</sup> Figure 9 depicts the cylindrical block, which is 70 mm in diameter and 80 mm long. Embedded in the phantom 15 mm from its central axis are three cylindrical inhomogeneities of 8 mm diameter with the following coefficients relative to the surrounding medium: (A)  $1 \times \mu_a$  and  $5 \times \mu'_s$ , (B)  $5 \times \mu_a$  and  $1 \times \mu'_s$  and (C)  $2 \times \mu_a$  and  $2 \times \mu'_s$ . A preliminary result using the same phantom has been reported<sup>22</sup> which employed just eight physical detector channels and for which only two source fibers were available, requiring manual rotation of the phantom. The results presented here represent the first obtained since completion of the system, in that all 32 source and detector channels are utilized, the VOAs are integrated, and the data acquisition is performed fully automatically without the need to manually rotate the fiber holder ring. These measures have resulted in considerable improvements in data collection efficiency, acquisition speed and ease of use of the instrument, which are all crucial features of a clinical imaging instrument.

### A. Image data acquisition

All 32 source fibers and 32 detector fiber bundles were arranged uniformly around the circumference of the object

and held in position by a black plastic ring (see Fig. 9). The experiment was automatically executed under computer control according to a pre-defined data acquisition protocol. The laser power applied to the phantom surface was approximately 1 mW, and data were recorded at a single wavelength  $\lambda = 800$  nm. The acquisition time per source position was arbitrarily chosen to be 30 s although this could have been significantly shorter since the recorded signal was more than adequate. VOAs were employed to equalize the detected intensities. Five detector channels on either side of the activated source were completely shut off in order to satisfy the finite dynamic range of the VOAs. However, it has been established from previous experiments that, for this type of phantom, data from small source-detector separations provide very little useful image information anyway. This acquisition geometry is equivalent to a fan beam configuration with each activated source opposed by 22 active detector channels, resulting in a total of  $32 \times 22 = 704$  measurements (TPSFs). The 22 TPSFs recorded for one source are shown in Fig. 10.

## B. Data pre-processing

As a consequence of the need to minimize the forward model calculation in the reconstruction scheme, the imaging algorithm is provided with data in the form of a basis consisting of various characteristics of the TPSFs. These so-called data types can currently consist of any combination of temporal moments (around zero), central moments (around the mean), normalized Laplace and Mellin-Laplace transforms and integrated intensity.<sup>23</sup> An appropriate choice of data types is required for simultaneously reconstructing separate absorption and scattering profiles.<sup>24</sup> The mean flight time, variance about the mean and Laplace transform (with a coefficient of  $0.005 \text{ ps}^{-1}$ ) were chosen in this experiment.

Noise, reflections, cross talk, the finite width and asymmetry of the IRF and other effects all produce systematic errors in the recorded TPSFs and consequently contaminate the derived data types. In order to reduce systematic errors in the raw data the following pre-processing methods were performed.

- (1) *Windowing and background subtraction.* A suitable temporal window (i.e., part of the full data acquisition span) is chosen from which the data types are computed. Thereby the pre-peak due to the ‘‘source cross talk,’’ discussed in Sec. IV D, can be effectively removed and it is ensured that a consistent region is sampled in all TPSFs. Any background noise due to low-level stray light is subsequently subtracted.
- (2) *Calibration and IRF correction.* Calibration and correction for the finite temporal response of the system is dependent on the data type being calculated. For mean time data the full set of temporal response measurements for all sources and detectors (described in Sec. III) allows the calibration of the temporal offset due to differences in fiber and cable lengths, etc. The same measurements are also used to correct errors in the mean time due to the particular IRF characteristics (asymmetry, reflection, etc). Similarly, these IRF characteristics also af-

fect the variance, and are corrected for by using calibration values derived from the variances of the IRFs. The Laplace transform data are calculated relative to the mean times of the respective TPSFs.

- (3) *Two-dimensional (2D)/three-dimensional (3D) correction.* A correction is performed on the measurement data to account for the fact that the image reconstruction is based on a 2D forward model of the cylindrical phantom. An analytically derived correction factor specific to each data type is used to scale the experimental values to closer match the simulated 2D forward data in the image reconstruction algorithm. One benefit of the 2D/3D correction is that it reduces ring artifacts in the reconstructed images.

A full description of these calibration methods was provided by Hillman *et al.*<sup>25</sup>

## C. Image reconstruction

A dedicated image reconstruction software package, known as TOAST (temporal optical absorption and scattering tomography), has been developed at UCL.<sup>26,27</sup> It employs measurements extracted from TPSFs recorded for a number of source-detector pairs to compute tomographic 2D or 3D images of the absorption and scattering profiles of any highly scattering object. The algorithm is based on a finite element (FEM) diffusion light transport forward model and an iterative reconstruction solver. General methods in optical tomography have been reviewed by Arridge.<sup>28</sup>

The 2D/3D correction of the measurement data, combined with the cylindrical symmetry of the phantom and the fact that the optodes were arranged in a single plane, enabled TOAST to employ a computationally faster 2D reconstruction. Using the three types of measurement data (mean time, variance and Laplace transform) described in Sec. V B, and starting with homogeneous background values of  $\mu_a = 0.01$  and  $\mu_s' = 1.0$ , the absorption and scattering maps of the phantom's cross section were simultaneously reconstructed. The circular FEM mesh used in the forward solver consisted of 7392 triangular elements, and the image was reconstructed into a  $16 \times 16$  pixel basis. The Robin boundary condition was used with the nonlinear conjugate gradient method and median filtering after each update. No regularizing schemes were employed, and no further improvement in the image quality was observed after 17 iterations. The corresponding absorption and scattering images are shown in Fig. 11, and clearly reveal the three embedded perturbers at their expected locations. The absorption image is dominated by region B, while region A is clearly revealed in the scattering map. The weaker region, C, can be identified in both images. Although the separation of the absorption and scattering profiles is good there is some identifiable cross talk, noticeably in the scattering image. This cross talk and the inherently lower resolution of the absorption image are due to the choice of data types. There are also some artifacts present, especially a ring artifact in the absorption map. These images are purely qualitative, but it should be stressed that they are absolute images which were obtained without any reference

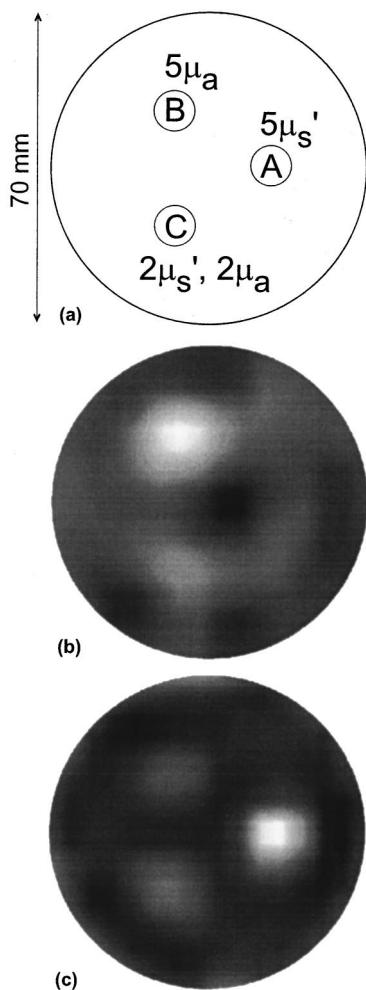


FIG. 11. Cross section of the phantom indicating the three regions of interest (a) and the reconstructed absorption (b) and scattering (c) profiles. The scales of the reconstructed images are arbitrary.

measurements (i.e., without a measurement of the object minus the perturbers) from purely time-resolved data.

## VI. DISCUSSION

A novel 32-channel time-resolved medical optical tomography system has been constructed and evaluated. We have demonstrated that very high temporal resolution ( $\sim 100$  ps) and stability ( $\sim 5$  ps) can be achieved reliably over an extended period of time, and no dedicated reference channel is required. Rapid acquisition of image data with up to  $\sim 300\,000$  cps per channel is performed automatically under computer control. We present for the first time results obtained with the completed instrument. Separate tomographic images of the internal absorption and scattering properties of a tissue equivalent phantom were successfully reconstructed from purely time-resolved data without the need for difference measurements.

The basic hardware of the instrument has been completed. However, future additions to the system will ultimately include a portable and rugged two-wavelength laser system that will enable us to perform studies in a hospital environment. One example of an appropriate technology is the fiber laser, such as the commercially available Femtolite

780 (IMRA America, Ann Arbor, MI). A portable laser will also be required to provide a fast and stable reference signal, which is currently derived from an external photodiode. A new variable optical attenuator allowing computer control of the source intensity will be integrated into the system shortly. A "helmet" suitable for safely holding 32 source and detector optodes arranged over the surface of the head of a neonate is in the process of being designed, and will facilitate collection of data over a 3D volume.

Nonimaging NIR spectroscopy measurements are being performed routinely for extended bedside monitoring lasting up to several hours. Similarly, this imaging system has been designed primarily as a continuous bedside monitor, with the images expected to be updated at intervals of several minutes. Full iterative image reconstruction is currently performed off line, and for large mesh sizes it can take several minutes. However, it is envisaged that preliminary images can be reconstructed more rapidly during the experiment. This may be accomplished using a low resolution iterative scheme or, perhaps a modified backprojection algorithm, such as has been employed in electrical impedance tomography (EIT).<sup>29</sup>

Our ongoing program of research includes the continuous evaluation and optimization of the performance of each element in the imaging process and the study of means of improving image quality and quantitative accuracy. Investigations using more complex (3D) phantoms are currently underway,<sup>30</sup> and initial clinical trials at the UCL neonatal intensive care unit will follow soon. Absorption images recorded at two wavelengths (typically 780 and 820 nm) should then allow blood volume and oxygenation within the tissue to be estimated, and changes thereof to be detected. Another benefit of using a two-wavelength system may be that when the *ratio* of intensities at two wavelengths is recorded in rapid succession, many of the systematic errors associated with continuous intensity measurements cancel out, thus providing a useful and robust additional data type.

Although the principal application of the new imaging system is in the monitoring of premature babies, other potential medical applications include (i) the monitoring of brain injuries occurring at child birth for *term* babies (birth asphyxia), (ii) topographic mapping of the adult cortex (tomographic imaging of the adult head is probably not feasible because of its large size, and hence excessive attenuation of light), and (iii) optical mammography, which may one day provide a safe and comfortable (no compression of the breast is required) way of detecting or specifying breast disease at an early stage. The techniques developed as part of this research may also aid the development of new industrial applications where imaging through strongly scattering media is required.

Data obtained with this system, the image reconstruction software and information on exchanging phantoms are available on our website.<sup>31</sup>

## ACKNOWLEDGMENTS

The authors would like to thank Dr. Simon Arridge and Dr. Martin Schweiger for their assistance with the image

reconstruction. This research was generously funded by the Wellcome Trust and Hamamatsu Photonics. One of the authors (F.E.W.S.) gratefully acknowledges the support of a UCL graduate school scholarship.

- <sup>1</sup>R. Bright, *Case CCV*, Longman, Rees, Orms, Brown and Green, Paternoster Row, London **II**, 431 (1831).
- <sup>2</sup>F. F. Jöbsis, *Science* **198**, 1264 (1977).
- <sup>3</sup>M. Cope and D. T. Delpy, *Med. Phys.* **26**, 289 (1988).
- <sup>4</sup>D. T. Delpy and M. Cope, *Philos. Trans. R. Soc. London, Ser. B* **352**, 649 (1997).
- <sup>5</sup>J. C. Hebden, S. R. Arridge, and D. T. Delpy, *Phys. Med. Biol.* **42**, 825 (1997).
- <sup>6</sup>S. R. Arridge and J. C. Hebden, *Phys. Med. Biol.* **45**, 841 (1997).
- <sup>7</sup>A. Maki, Y. Yamashita, Y. Ito, E. Watanabe, Y. Mayanagi, and H. Koizumi, *Opt. Lett.* **22**, 1997 (1995).
- <sup>8</sup>B. Chance, Q. Luo, S. Nioka, D. C. Alsop, and J. A. Detre, *Philos. Trans. R. Soc. London, Ser. B* **352**, 707 (1997).
- <sup>9</sup>S. B. Colak, D. G. Papaioannou, G. W. t'Hooft, M. B. van der Mark, H. Schomberg, J. C. J. Paasschens, J. B. M. Melissen, and N. A. A. J. van Asten, *Appl. Opt.* **36**, 180 (1997).
- <sup>10</sup>H. Jiang, K. D. Paulsen, U. L. Osterberg, B. W. Pogue, and M. S. Patterson, *Opt. Lett.* **20**, 2128 (1995).
- <sup>11</sup>M. Kaschke, H. Jess, G. Gaida, J.-M. Kaltenbach, and W. Wrobel, *OSA Proc. Adv. Opt. Imaging Photon Migration* **21**, 88 (1994).
- <sup>12</sup>J. P. Van Houten, D. A. Benaron, S. Spilman, and D. K. Stevenson, *Pediatr. Res.* **39**, 470 (1996).
- <sup>13</sup>J. C. Hebden, D. J. Hall, M. F. Firbank, and D. T. Delpy, *Appl. Opt.* **34**, 8038 (1995).
- <sup>14</sup>M. Oda *et al.*, *Proc. SPIE* **2979**, 765 (1997).
- <sup>15</sup>V. Ntziachristos, X. Ma, A. G. Yodh, and B. Chance, *Rev. Sci. Instrum.* **70**, 193 (1999).
- <sup>16</sup>H. Rinneberg, D. Grosenick, H. Wabnitz, H. Danlewski, K. Moesta, and P. Schlag, *OSA TOPS Adv. Opt. Imaging Photon Migration* **21**, 278 (1998).
- <sup>17</sup>G. Müller *et al.*, **IS11** (SPIE, Bellingham, WA, 1993).
- <sup>18</sup>K. Wells, J. C. Hebden, F. E. W. Schmidt, and D. T. Delpy, *Proc. SPIE* **2979**, 599 (1997).
- <sup>19</sup>F. E. W. Schmidt, M. E. Fry, J. C. Hebden, and D. T. Delpy, *OSA TOPS Adv. Imaging Photon Migration* **21**, 120 (1998).
- <sup>20</sup>M. Lampton and R. Raffanti, *Rev. Sci. Instrum.* **65**, 3577 (1994).
- <sup>21</sup>M. F. Firbank, M. Oda, and D. T. Delpy, *Phys. Med. Biol.* **40**, 955 (1995).
- <sup>22</sup>J. C. Hebden, F. E. W. Schmidt, M. E. Fry, M. Schweiger, E. M. C. Hillman, and D. T. Delpy, *Opt. Lett.* **24**, 534 (1999).
- <sup>23</sup>M. Schweiger and S. R. Arridge, *Phys. Med. Biol.* **44**, 1699 (1999).
- <sup>24</sup>S. R. Arridge and W. R. B. Lionheart, *Opt. Lett.* **23**, 882 (1998).
- <sup>25</sup>E. M. C. Hillman, J. C. Hebden, F. E. W. Schmidt, S. R. Arridge, M. S. Schweiger, and D. T. Delpy, *Appl. Opt.* (submitted).
- <sup>26</sup>M. Schweiger and S. R. Arridge, *OSA TOPS Adv. Opt. Imaging Photon Migration* **2**, 263 (1996).
- <sup>27</sup>TOAST website: <http://www.medphys.ucl.ac.uk/research/borg/toast/index.htm>.
- <sup>28</sup>S. R. Arridge, *Inverse Probl.* **15**, R41 (1999).
- <sup>29</sup>K. Boone, D. Barber, and B. Brown, *J. Med. Eng. Technol.* **21**, 201 (1997).
- <sup>30</sup>S. R. Arridge, J. C. Hebden, M. Schweiger, F. E. W. Schmidt, M. E. Fry, E. M. C. Hillman, H. Dehghani, and D. T. Delpy, *Int. J. Imaging Syst. Technol.* (submitted).
- <sup>31</sup>BORG website: <http://www.medphys.ucl.ac.uk/research/borg>.